MICROSCOPY

Microscopy, 2017, 1–8
doi: 10.1093/jmicro/dfx031

Article

Applicability of non-linear imaging in high-resolution transmission electron microscopy

Yunjie Chang[1,2], Shouqing Li[1,2,3], Yumei Wang[1], and Binghui Ge[1,*]

[1]Beijing National Laboratory for Condensed Matter Physics, Institute of Physics, Chinese Academy of Sciences, Beijing 100190, China, [2]University of Chinese Academy of Sciences, Beijing, 100049, China, and [3]Department of physics, Beijing Normal University, Beijing, 100875, China

[*]To whom correspondence should be addressed. E-mail: bhge@iphy.ac.cn

Received 13 June 2017; Editorial Decision 4 August 2017; Accepted 9 August 2017

Abstract

According to transmission cross-coefficient theory, the information limit of non-linear imaging in high-resolution transmission electron microscopy is, under certain conditions, far beyond that of linear imaging, which suggests the possibility of using high-frequency information for structural determination. In this article, we studied the information beyond the linear information limit by means of multislice method simulation, with AlN as an example, and more structural information was obtained by using part of the high-frequency information.

Key words: High-resolution transmission electron microscopy, Non-linear imaging, Information limit, Transmission cross-coefficient theory, Quasi-achromatic condition

Introduction

High-resolution transmission electron microscopy (HRTEM) is a powerful technique to investigate crystal structures. A widely used performance criterion in HRTEM is the information limit of the electron microscope, which is defined as the inverse of the highest spatial frequency that can be transferred by the imaging system from the exit plane to the image plane. It is important, however, that this one-to-one relationship between the information limit and attainable resolution applies only in the case of linear imaging with negligible non-linear interference, which means that specimens must be very thin, i.e. weak-phase objects.

The contrast transfer function (CTF) of electron microscopes was thoroughly investigated through transmission cross-coefficient (TCC) theory by K. Ishizuka in 1980 [1], and he found the information limits for linear and non-linear interferences to be different. More interesting are the experiments with Young's fringes carried out by J. Barthel and A. Thust, in which the highest detected frequencies in diffractograms was found to extend even beyond the highest transfer frequency of the inserted objective aperture [2], indicating that the information limit of traditional linear imaging is not enough to explain information transfer by optical systems, because significant non-linear information is present in the higher frequencies of the diffractogram [3,4]. Later, S. Van Aert *et al.* [5] derived the closed analytical forms of the information limit for linear and non-linear information through channeling theory, assuming zero spherical aberration. Their results show that the information

limit for the non-linear component may be $\sqrt{2}$ times larger than the information limit for the linear one.

Since there is much space between the non-linear structural information limit and the linear information limit, a question comes up: whether the non-linear information can be used to determine structure. In the present work, the non-linear imaging component was investigated based on multislice simulation of wurtzite-structure AlN as an example. Results show that in some special cases, the phases of some high-frequency non-linear information may give a good indication of the phases of structure factors, which can be used to deduce the structure.

Information limit of linear and non-linear components

First, we briefly introduce TCC theory and demonstrate the difference between the information limits of linear and non-linear imaging components. More details can be found in Refs. [1,6–8].

According to TCC theory, the Fourier transform of the image intensity, i.e. the diffractogram, will be

$$\begin{aligned} I_{\mathrm{im}}(\vec{K}) &= \int T(\vec{K'}, \vec{K'}-\vec{K})Q(\vec{K'})Q^*(\vec{K'}-\vec{K})d\vec{K'} \\ &= \int_{\vec{K'}} |Q(\vec{K'})|^2 d\vec{K'} + T(\vec{K}, 0)O(\vec{K}) \\ &\quad + T(0, -\vec{K})O^*(-\vec{K}) \\ &\quad + \int_{\vec{K'}\neq\vec{K}, \vec{K'}\neq 0} T(\vec{K'}, \vec{K'}-\vec{K})O \\ &\quad (\vec{K'})O^*(\vec{K'}-\vec{K})d\vec{K'} \\ &= I_0(\vec{K}=0) + I_1(\vec{K}\neq 0) + I_2(\vec{K}\neq 0), \end{aligned} \tag{1}$$

in which '$\vec{K}$' represents the two dimensional vector in reciprocal space, '*' represents the conjugate form, $Q(\vec{K'})$ is the diffracted wave, and $O(\vec{K})$ is the Fourier transform of the object function, $T(\vec{K'}, \vec{K'}-\vec{K})$ is the transmission cross coefficient, a complex function that depends on the temporal and spatial coherence of the microscope as well as the spherical aberration C_s and, the defocus of the objective lens, etc.

$$I_0(\vec{K}=0) = \int_{\vec{K'}} |Q(\vec{K'})|^2 d\vec{K'} \tag{2}$$

$$I_1(\vec{K}\neq 0) = T(\vec{K}, 0)O(\vec{K}) + T(0, -\vec{K})O^*(-\vec{K}) \tag{3}$$

$$\begin{aligned} I_2(\vec{K}\neq 0) = \int_{\vec{K'}\neq\vec{K}, \vec{K'}\neq 0} & T(\vec{K'}, \vec{K'}-\vec{K})O(\vec{K'}) \\ & O^*(\vec{K'}-\vec{K})d\vec{K'} \end{aligned} \tag{4}$$

Here, $I_0(\vec{K}=0)$ represents the transmitted electron beam, $I_1(\vec{K}\neq 0)$ represents the linear interference between the transmitted beam and one of the diffracted electron beams, and $I_2(\vec{K}\neq 0)$ represents the non-linear interference between two diffracted beams, $\vec{K'}$ and $\vec{K'}-\vec{K}$.

To get the analytical expression of $I_1(\vec{K}\neq 0)$ and $I_2(\vec{K}\neq 0)$, an object function $O(\vec{K})$ based on the pseudo-weak-phase object approximation (PWPOA) was input into Eqs. (3)–(4) [8]. Then

$$I_1(\vec{K}\neq 0) = 2\sigma E_\delta(\vec{K}, 0)E_\alpha(\vec{K}, 0)F(\vec{K})S(\vec{K})\sin(\chi_{\mathrm{eff}}(\vec{K})), \tag{5}$$

And

$$\begin{aligned} I_2(\vec{K}\neq 0) = {} & \sigma^2 E_\delta^x E_\alpha^x F(\vec{K'_x})F(\vec{K}-\vec{K'_x})S(\vec{K'_x})S(\vec{K'_x}-\vec{K}) \\ & \times\cos\{\chi_{\mathrm{eff}}(\vec{K'_x}) - \chi_{\mathrm{eff}}(\vec{K'_x}-\vec{K})\}_{\vec{K'_x}=\frac{\vec{K}}{2}} \\ & + \sum_{\vec{K'_x}\neq\frac{\vec{K}}{2}} 2\sigma^2 E_\delta^x E_\alpha^x F(\vec{K'_x})F(\vec{K}-\vec{K'_x})S(\vec{K'_x}) \\ & \times S(\vec{K'_x}-\vec{K})\cos\{\chi_{\mathrm{eff}}(\vec{K'_x}) - \chi_{\mathrm{eff}}(\vec{K'_x}-\vec{K})\}, \end{aligned} \tag{6}$$

where E_δ, E_δ^x and E_α, E_α^x represent the damping envelopes of the temporal and spatial coherences, respectively; $F(\vec{K})$ represents the crystal structure factor; Δf_{eff} is the effective focus and $\chi_{\mathrm{eff}}(\vec{K})$ is the effective CTF [8]; and

$$S(\vec{K}) = \frac{\sin\left(\frac{\pi\lambda n\Delta z\vec{K}^2}{2}\right)}{\sin\left(\frac{\pi\lambda\Delta z\vec{K}^2}{2}\right)}, \tag{7}$$

where λ, n and Δz represent the electron wavelength, number of slices and slice thickness of the crystal, respectively.

From Eqs. (4), (6) and (7), it can be found that I_2 is summation of the non-linear interferences between various 'couples' of diffractions, i.e. $F(\vec{K'_x})$ and $F(\vec{K'_x}-\vec{K})$ for different $\vec{K'_x}$, and the weight of each non-linear interference depends on the imaging parameters and crystal thickness.

From Eqs. (5) and (6) the linear and non-linear damping envelopes due to temporal coherence of the electron source can be respectively expressed as [8]

$$E_\delta^l(\vec{K}) = E_\delta(\vec{K}, 0) = \exp\left\{-\frac{1}{2}(\pi\lambda D)^2\vec{K}^4\right\} \tag{8}$$

and

$$E_\delta(\vec{K'}, \vec{K'}-\vec{K}) = \exp\left\{-\frac{1}{2}(\pi\lambda D)^2[(\vec{K'})^2 - (\vec{K'}-\vec{K})^2]^2\right\}, \tag{9}$$

where 'D' represents the focus spread and the superscript 'l' means the linear information. The reciprocal spatial frequency $\vec{K}$ for $E_\delta^l(\vec{K}) = e^{-2}$ is used to define the conventional information limit and will be referred to as

'the linear information limit' in the following. When the non-linear components are concerned, the damping envelopes due to temporal coherence $E_\delta(\overrightarrow{K'}, \overrightarrow{K'} - \overrightarrow{K})$ (see Eq. (9)) obviously differ from $E_\delta^l(\overrightarrow{K})$, especially for high reciprocal spatial frequencies, just as shown in Fig. 1. That is, the information limit for non-linear information, referred to as 'non-linear information limit,' differs from the linear information limit.

The difference between $E_\delta(\overrightarrow{K'}, \overrightarrow{K'} - \overrightarrow{K})$ and $E_\delta^l(\overrightarrow{K})$ is easy to understand. According from Eq. (9), when $|\overrightarrow{K'}| = |\overrightarrow{K'} - \overrightarrow{K}|$ ($|\overrightarrow{K'}|$ represents the modulus of vector $\overrightarrow{K'}$), $E_\delta(\overrightarrow{K'}, \overrightarrow{K'} - \overrightarrow{K}) = 1$. This means the temporal coherence envelope takes its maximum value of unity along the perpendicular bisector of $\overrightarrow{K}$, as shown in Fig. 2, a phenomenon called the 'achromatic condition' [1] because the chromatic aberration effect disappears at this point.

Simply put, non-linear information limit is higher than the linear one, and the difference between them is due mainly to the achromatic condition for non-linear interference; thus the non-linear terms carry higher-resolution information. In the next section, wurtzite-structured AlN is taken as an example for the study of the non-linear component, and the possibility of using the non-linear component for determining structure is studied.

Application of the non-linear component

A schematic diagram of an AlN [100] diffractogram is shown in Fig. 3. As illustrated before, $I_1(\overrightarrow{K})$ is negligible at sufficiently high frequencies because of the strong damping of E_δ^l,; thus it is more appropriate to investigate the impact of $I_2(\overrightarrow{K})$ at high frequencies. Here, reflection 012, which lies just within the linear information limit (indicated by the dashed circle in Fig. 3), and reflection 013, which lies just beyond the linear information limit, are chosen as examples in our investigation. Moreover, as illustrated by X.D. Zou *et al.* [9], good phases are more important than amplitudes for determining atomic column positions, so in the following, the phase of the reflections 012 and 013 will be studied by means of dynamic simulation with varied imaging conditions and varied thickness.

The simulations of AlN HRTEM images are carried out along the [100] direction. In this direction, the Al and N atoms do not overlap, and the atomic distance between adjacent Al and N atoms is about 1.09 Å. The slice thickness (Δz) of AlN in the [100] direction is 3.11 Å; the radius of the objective aperture is set as 2 $Å^{-1}$. Imaging parameters with different effective defocus values around the Scherzer focus, as shown in Table 1, are chosen for simulations. Actually, these imaging parameters correspond to a

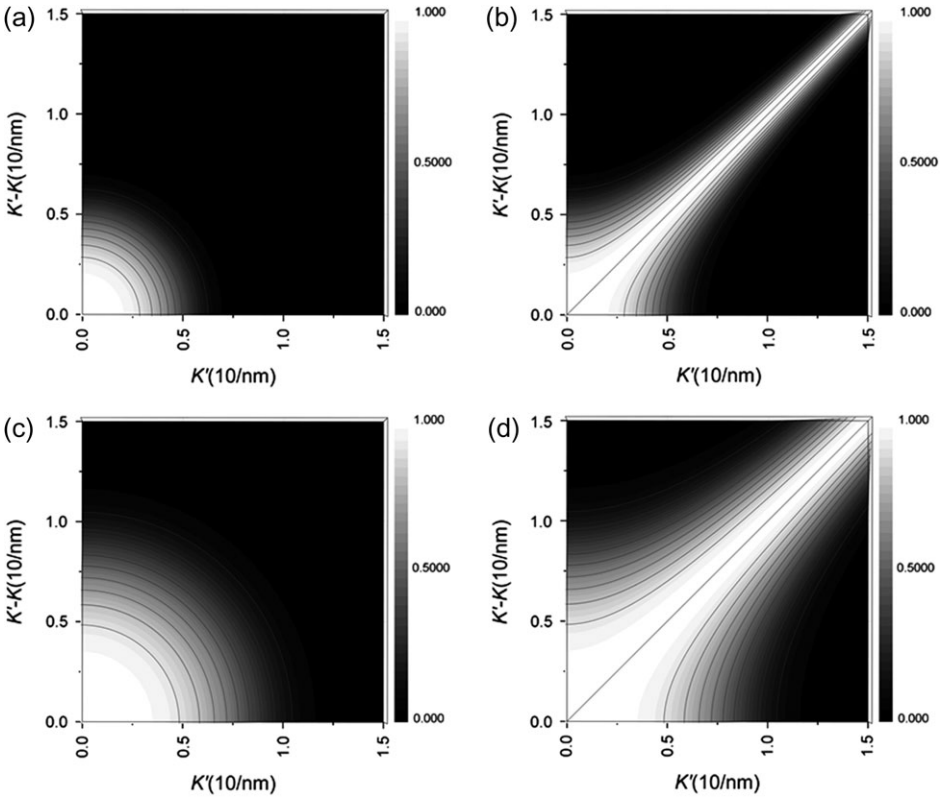

Fig. 1. Temporal envelopes for (a) linear, (b) non-linear imaging components with $D = 7\ nm$ and (c) linear, (d) non-linear imaging components with $D = 2.5\ nm$ of microscope with $E = 200\ kV$, respectively. Only one quadrant of $(\overrightarrow{K'}, \overrightarrow{K'} - \overrightarrow{K})$ space is shown.

JEOL-2010 microscope, which is equipped with a LaB_6 filament and has a linear information limit 0.6 $Å^{-1}$ (i.e. about 1.6 Å). Phases of reflections in the diffractogram were obtained from the Fourier transforms of the simulated images, and the phases of the non-linear component were obtained by separating the linear and non-linear components [8].

Figure 4(a) shows the variation of $\alpha\{I_{im}(012)\} - \alpha\{F(012)\}$, the phase difference between reflection 012 in the diffractogram and the corresponding structure factor, over crystal thickness under different effective defocus values Δf_{eff}. When the crystal is thin, it varies with the sign of $\sin(\chi_{\text{eff}}(\vec{K}))$ for $\vec{K} = 012$ as indicated in Eq. (5) (note that $S(\vec{K})$ for $\vec{K} = 012$ remains positive throughout our simulation range ($n \leq 31$), according to Eq. (7)), because $I_2(\vec{K})$ is negligible, as shown in Fig. 4(e), and

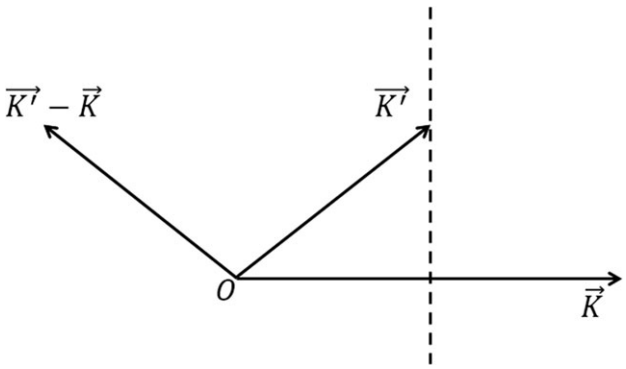

Fig. 2. Diagram of achromatic condition for $E_\delta(\vec{K'}, \vec{K'} - \vec{K})$. The dashed line represents the perpendicular bisector of vector $\vec{K}$.

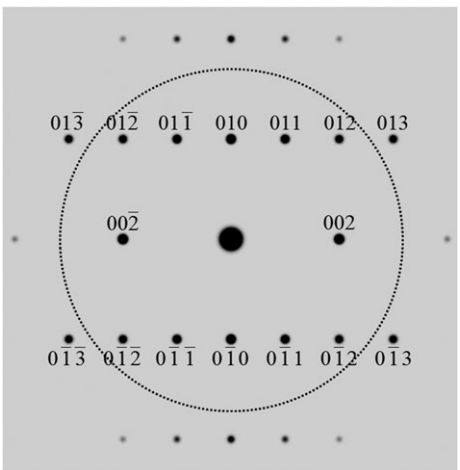

Fig. 3. Schematic of AlN [100] diffractogram. The dotted circle indicates the frequency of 0.6 $Å^{-1}$.

$ln\left(\frac{|I_2(012)|}{|I_1(012)|}\right) < 0$, meaning that $I_{im}(\vec{K}) \approx I_1(\vec{K})$. With the crystal getting thicker, $\alpha\{I_{im}(012)\} - \alpha\{F(012)\}$ becomes independent of defocus when AlN thickness is above 4.67 nm (15 slices), because $\{I_2(012)\}$ becomes dominant in $\{I_{\text{im}}(012)\}$; i.e. $\left(ln(\frac{|I_2(012)|}{|I_1(012)|}\right)$ becomes positive as shown in Fig. 4(e)). More interesting is that $\alpha\{I_{im}(012)\}$, i.e. $\alpha\{I_2(012)\}$, becomes approximately constant, and is almost equal to $\alpha\{F(012)\}$,; as shown by Fig. 4(c), $\alpha\{I_2(012)\} - \alpha\{F(012)\}$.

Similar to reflection 012, $\alpha\{I_{\text{im}}(013)\} - \alpha\{F(013)\}$ varies with the sign of $\sin(\chi_{\text{eff}}(\vec{K}))$ when the crystal is thin, as shown in Fig. 4(b), and remains constant with the crystal getting thicker. Furthermore, because reflection 013 is beyond the linear information limit while 012 is not, $\alpha\{I_2(013)\}$ becomes dominant more quickly, as shown Fig. 4(e) and (f); thus $\alpha\{I_{\text{im}}(013)\} - \alpha\{F(013)\}$ approaches a constant value more quickly than does $\alpha\{I_{\text{im}}(012)\} - \alpha\{F(012)\}$, as shown in Fig. 4(b). For $\alpha\{I_{\text{im}}(013)\} - \alpha\{F(013)\}$ remains constant and is not far from zero when sample thickness is above 1.55 nm, indicating that $\alpha\{I_2(013)\}$, i.e. $\alpha\{I_{\text{im}}(013)\}$, may reflect the structure factor to some extent (see Fig. 4(d)). In the following we use the phase of $I_{\text{im}}(013)$, which is beyond the information limit, to try to recognize the species of Al and N.

Simulated images of AlN in the [100] zone axis with different thicknesses under $\Delta f_{\text{eff}} = -41$nm are shown in Fig. 5(b)–(f). Just like the image deconvolution [10], the phase of the artificial structure factor $\alpha\{F'(\vec{K})\}$ can be set equal to $\alpha\{I_{\text{im}}(\vec{K})\} - \pi$, i.e. $\alpha\{I_1(\vec{K})\} - \pi$, for reflections 010, 002, 011, and $\alpha\{F'(012)\}$ is set to be $\alpha\{I_{\text{im}}(012)\}$ according to their CTF values, and $\alpha\{F'(013)\}$ is set to be $\alpha\{I_{\text{im}}(013)\}$ because $\alpha\{I_{\text{im}}(013) \approx \alpha\{F(013)\}\}$; then we can get $\alpha\{F'(\vec{K})\}$ from $\vec{K} = 010$ to $\vec{K} = 013$ from the diffractogram of the simulated image. With the amplitudes of $I_{\text{im}}(\vec{K})$ retained, artificial potential maps can be obtained with atomic columns appearing as black dots by converting all $\alpha\{I_{\text{im}}(\vec{K})\}$ into $\alpha\{F'(\vec{K})\} + \pi$, as shown in Fig. 5 (h)–(l), corresponding to Fig. 5(b)–(f), respectively. As shown by Fig. 5(m)–(r), the intensity profiles corresponding respectively to the framed areas in Fig. 5(g)–(l), the 'Al' and 'N' atomic columns can be separated in the 'Al-N' dumbbell when the crystal thickness is above 4 nm. This means that the application of $I_{\text{im}}(013)$ does help us get structure details with resolution better than the linear information limit for the simulated linear information limit is about 1.6 Å, not enough to separate the dumbbell.

Table 1. Imaging parameters used for simulation. The effective defocus value ranges from −31 to −51 nm with 2 nm steps

E (kV)	α (mrad)	C_S (mm)	Defocus spread (nm)	Scherzer focus (nm)	Δf_{eff} (nm)	Linear information limit ($Å^{-1}$)
200	0.5	0.5	7	−41	−31:−2:−51	0.6

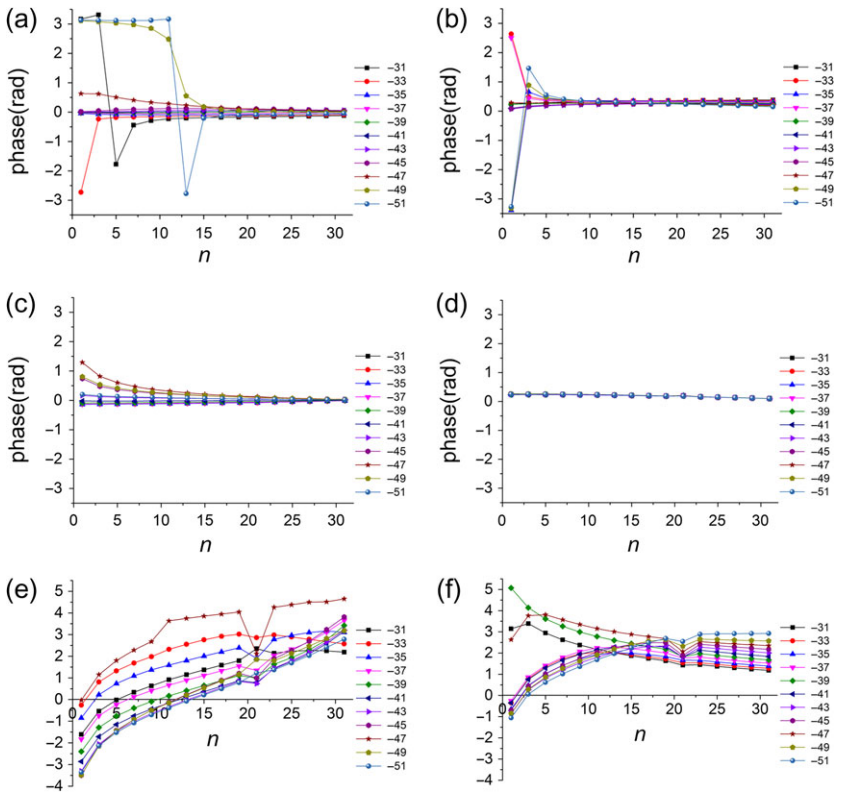

Fig. 4. Variation of phase differences over crystal thickness for different effective focus values Δf_{eff}. (a) $\alpha\{I_{im}(012)\} - \alpha\{F(012)\}$, (b) $\alpha\{I_{im}(013)\} - \alpha\{F(013)\}$, (c) $\alpha\{I_2(012)\} - \alpha\{F(012)\}$, (d) $\alpha\{I_2(013)\} - \alpha\{F(013)\}$, (e) $ln\left(\frac{|I_2(012)|}{|I_1(012)|}\right)$ and (f) $ln\left(\frac{|I_2(013)|}{|I_1(013)|}\right)$. "$n$" represents the number of slices, and slice thickness $\Delta z =$ 3.11 Å.

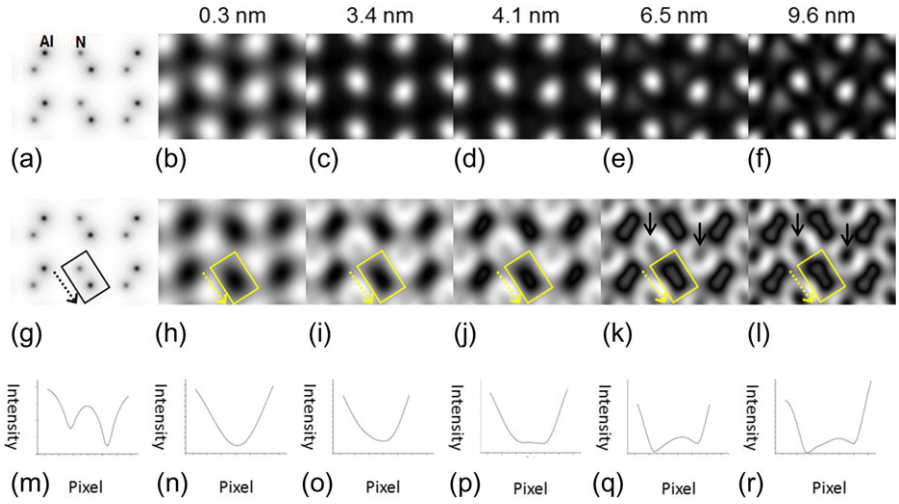

Fig. 5. (a) and (g) Projected potential maps of AlN [100] with atoms shown as black dots; (b)–(f) simulated images of AlN [100] with different thicknesses under $\Delta f_{\text{eff}} = -41$ *nm* (other imaging parameters are the same as shown in Table 2); (h)–(l) resulted maps corresponding to (b)–(f) by converting $\alpha\{I_{im}(\vec{K})\}$ to $\alpha\{F(\vec{K})\}$, respectively; solid arrows in (k) and (l) indicate extra bright contrasts that do not correspond to atomic columns. (m)–(r) Intensity profiles of the framed areas in (g)–(l), respectively, along the direction indicated by dotted arrows.

In addition, note that 'N' columns are lighter than 'Al' columns in the resulting maps shown in Fig. 5(j), but become darker than 'Al' in Fig. 5(k) and (l). This phenomenon, i.e. light atomic columns appearing with lower contrast than heavy ones in thin samples may appear darker when sample thickness is above a critical value, accords with the image

contrast variation illustrated in PWPOA [11], and can help us in atomic species recognition [12,13]. Besides, some extra areas of contrast, indicated by arrows, do not correspond to atomic columns but arise from strong non-linear information when the sample is thick [8].

Moreover, note that the distance between the Al and N atoms in the reconstructed map shown in Fig. 5 is not exactly same as that in the potential map, and similarly, the contrast in the reconstructed map is not linear with the atomic number, which is due to two reasons: first, the highest-frequency reflection used in the reconstruction, 013 (which has the reciprocal spatial frequency of 0.708 $Å^{-1}$), is not enough to separate the dumbbell with the Al-N interatomic distance 1.09 Å; second, the amplitudes and phases of the reflections in the diffractogram we used are not exactly equal to those of the corresponding structure factors. Even so, with the help of PWPOA and the nonlinear contribution, more structural information can be obtained.

Briefly, if we know the examined crystal structure, like in the previously shown example of AlN, we can directly determine whether the phase of high-frequency reflections accords with the phase of the structure factor, in an appropriate range of defocus and sample thickness. If the answer is positive, $\alpha\{I_2(\vec{K})\}$ may be used for structural determination, for instance, determination of polarity here; thus more structural information can be obtained.

Discussion

So far, the origin of this phenomenon, i.e. $\alpha\{I_2(\vec{K})\} \approx \alpha\{F(\vec{K})\}$ in AlN when the crystal is not thin, is still not clear. Here, we try to understand it by means of Cochran's equation [14],

$$\alpha\{F(\vec{K})\} \approx \alpha\{F(\overrightarrow{K'})\} + \alpha\{F(\vec{K} - \overrightarrow{K'})\}, \tag{10}$$

which means that the structure factors $F(\vec{K})$, $F(\overrightarrow{K'_x})$ and $F(\vec{K} - \overrightarrow{K'_x})$ may accord with a special relation in some cases, e.g. in certain projections of a crystal with simple structure or a protein crystal [14].

If we consider only the 'quasi-achromatic condition,'[6] i.e. $|\vec{K'_x}| \approx |\vec{K'_x} - \vec{K}|$, meaning that $\vec{K'_x}$ is adjacent to the perpendicular bisector of $\vec{K}$ (see Fig. 2), we can make approximations as

$$S(\overrightarrow{K'_x}) = \frac{\sin\left(\frac{\pi\lambda n\Delta z\,\overrightarrow{K'_x}^2}{2}\right)}{\sin\left(\frac{\pi\lambda\Delta z\,\overrightarrow{K'_x}^2}{2}\right)} \approx S(\vec{K'_x} - \vec{K}) = \frac{\sin\left(\frac{\pi\lambda n\Delta z(\vec{K'_x} - \vec{K})^2}{2}\right)}{\sin\left(\frac{\pi\lambda\Delta z(\vec{K'_x} - \vec{K})^2}{2}\right)} \tag{11}$$

and

$$\cos\{\chi_{\text{eff}}(\overrightarrow{K'_x}) - \chi_{\text{eff}}(\overrightarrow{K'_x} - \vec{K})\} \approx 1. \tag{12}$$

Then $I_2(\vec{K})$ (see Eq. (6)) can be simplified as

$$\begin{aligned} I_2(\vec{K}) &= \sigma^2 E_\delta^x E_\alpha^x F(\overrightarrow{K'_x}) F(\vec{K} - \overrightarrow{K'_x}) S^2(\overrightarrow{K'_x})|_{\overrightarrow{K'_x}=\frac{\vec{K}}{2}} \\ &\quad + \textstyle\sum_{\overrightarrow{K'_x}\neq\frac{\vec{K}}{2}} 2\sigma^2 E_\delta^x E_\alpha^x F(\overrightarrow{K'_x}) F(\vec{K} - \overrightarrow{K'_x}) S^2(\overrightarrow{K'_x}) \\ &= A_x \times \left\{ F(\overrightarrow{K'_x}) F(\vec{K} - \overrightarrow{K'_x})\Big|_{\overrightarrow{K'_x}=\frac{\vec{K}}{2}} \right. \\ &\quad \left. + \textstyle\sum_{\overrightarrow{K'_x}\neq\frac{\vec{K}}{2}} 2F(\overrightarrow{K'_x}) F(\vec{K} - \overrightarrow{K'_x}) \right\}, \end{aligned} \tag{13}$$

where

$$A_x = \sigma^2 E_\delta^x E_\alpha^x S^2(\overrightarrow{K'_x}). \tag{14}$$

Then, according to Cochran's equation (see Eq. (10)) and the simplified $I_2(\vec{K})$ (see Eq. (13)), and considering that A_x is a non-negative value, the phase of $I_2(\vec{K})$ can reflect the phase of $F(\vec{K})$, i.e.

$$\alpha\{I_2(\vec{K})\} \approx \alpha\{F(\vec{K})\}. \tag{15}$$

Nevertheless, it should be pointed out that $\alpha\{I_2(\vec{K})\} \approx \alpha\{F(\vec{K})\}$ can be found, up to now, only for non-aberration-corrected TEM imaging, because the non-linear component is the summation of the non-linear interferences between various 'couples' of reflections, and things that are simpler for the non-aberration-corrected imaging of few reflections should be taken into consideration, as will be elucidated in the following.

Figure 6 shows the variations of $E_\delta(\vec{K'}, \vec{K'} - \vec{K})$ $E_\alpha(\vec{K'}, \vec{K'} - \vec{K})$ for $\vec{K}$ = 012 and 013 as a function of $\vec{K'}$, with Fig. 6(a) and (c) showing the non-aberration-corrected imaging case and Fig. 6(b) and (d) showing the aberration-corrected imaging case. As for our simulation in this work (refer to Fig. 6(a) and (c)), considering that 001 and 003 are distinction reflections and the linear information limit is 0.6 $Å^{-1}$ (which can be considered as a virtual aperture), Eq. (13) can be rewritten as

$$I_2(012) \approx A_x \times \{2F(010)F(002)\} \tag{16}$$

and

$$I_2(013) \approx A_x \times \{2F(011)F(002)\} \tag{17}$$

for reflections 012 and 013 in AlN, respectively. Therefore, it is clear that only when $\vec{K'}$ is adjacent to the perpendicular bisector of $\vec{K}$, should the non-linear interferences between beams $\vec{K'}$ and $\vec{K'} - \vec{K}$ be taken into consideration,

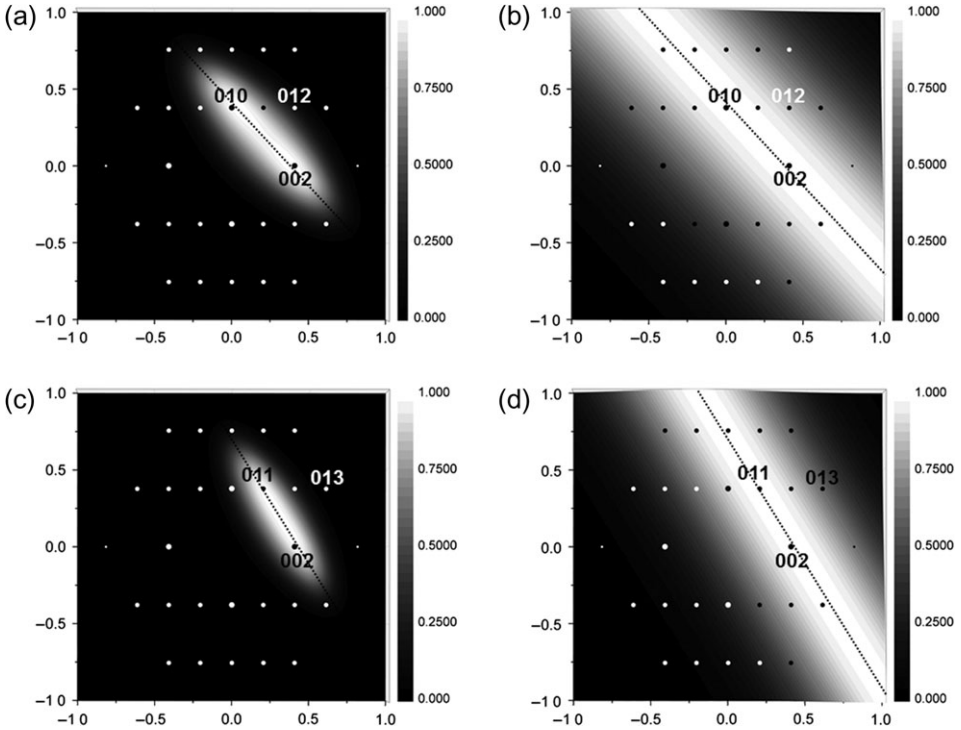

Fig. 6. Variations of $E_\delta(\vec{K'}, \vec{K'} - \vec{K})E_\alpha(\vec{K'}, \vec{K'} - \vec{K})$ for $\vec{K}$ = 012 ((a) and (b)) and 013 ((c) and (d)) under different imaging parameters: (a) and (c) C_S = 0.5mm, α = 0.5mrad and D = 7 nm, with Δf = −41nm (Scherzer focus); (b) and (d) C_S = 0.015mm, α = 0.05 mrad and D = 2.5 nm, with Δf = −7nm (Scherzer focus). AlN reflections are indicated by spots. The perpendicular bisectors of 012 and 013 are indicated by dotted lines.

which accords well with the approximation of the quasi-achromatic condition [6].

Comparing Fig. 6(a) and (b) or (c) and (d), it can be found that any decrease of the imaging parameters C_S, α and D, will contribute more non-linear interference for a specific reflection. In this case, therefore, the phase of $I_2(\vec{K})$ does not have a simple relation with the phase of $F(\vec{K})$, so it is hard for us to make use of it.

Briefly, the phase of the non-linear information of reflection 013 for AlN is found to be close to the phase of the structural factor under the non-aberration-corrected condition, so the non-linear information can be used directly in determining structure, and here the polarity of AlN was determined. Nevertheless, more work needs to be done to understand this phenomenon deeply.

Concluding remarks

The linear information limit and the non-linear information limit of HRTEM imaging differ significantly, which enables a question of whether the non-linear information is useful for structural determination, so in this paper the information beyond the linear information limit is studied by means of a multislice simulation with wurtzite-structured AlN as the model. For non-aberration-corrected imaging, the phase of the non-linear information of reflection 013 is found to be close to the phases of the structure factor when the sample is thick. With the help of the non-linear component, Al and N atoms in the projection of [110] can be separated, indicating that higher-resolution, even atomic-resolution, structural information can be obtained by conventional TEM. This paper offers a new way to employ non-aberration-corrected TEM, but such mechanisms in electron microscopy or crystallography remain open issues.

Funding

This work was supported by the National Natural Science Foundation of China (Grants No. 11374332, 11104327, and 11474329).

References

1. Ishizuka K (1980) Contrast transfer of crystal images in tem. *Ultramicroscopy* 5: 55–65.
2. Barthel J, and Thust A (2008) Quantification of the information limit of transmission electron microscopes. *Phys. Rev. Lett.* 101: 200801.
3. Haider M, Hartel P, Muller H, Uhlemann S, and Zach J (2010) Information transfer in a tem corrected for spherical and chromatic aberration. *Microsc. Microanal.* 16: 393–408.

4. Ishizuka K, and Kimoto K (2016) Why do we need to use three-dimensional (3d) fourier transform (ft) analysis to evaluate a high-performance transmission electron microscope (tem)? *Microsc. Microanal.* 22: 971–980.
5. Van Aert S, Chen J H, and Van Dyck D (2010) Linear versus non-linear structural information limit in high-resolution transmission electron microscopy. *Ultramicroscopy* 110: 1404–1410.
6. Coene W M J, Thust A, deBeeck M, and VanDyck D (1996) Maximum-likelihood method for focus-variation image reconstruction in high resolution transmission electron microscopy. *Ultramicroscopy* 64: 109–135.
7. Chen J H, Zandbergen H W, and Dyck D V (2004) Atomic imaging in aberration-corrected high-resolution transmission electron microscopy. *Ultramicroscopy* 98: 81–97.
8. Chang Y, Wang Y, Cui Y, and Ge B (2016) Investigation of non-linear imaging in high-resolution transmission electron microscopy. *Microscopy* 65: 465–472.
9. Zou X D, Sundberg M, Larine M, and Hovmoller S (1996) Structure projection retrieval by image processing of hrem images taken under non-optimum defocus conditions. *Ultramicroscopy* 62: 103–121.
10. Han F S, Fan H F, and Li F H (1986) Image processing in high-resolution electron microscopy using the direct method. Ii. Image deconvolution. *Acta Cryst. A* 42: 353–356.
11. Li F H, and Tang D (1985) Pseudo-weak-phase-object approximation in high-resolution electron-microscopy 0.1. Theory. *Acta Cryst. A* 41: 376–382.
12. Tang C Y, Li F H, Wang R, Zou J, Zheng X H, and Liang J W (2007) Atomic configurations of dislocation core and twin boundaries in 3c-sic studied by high-resolution electron microscopy. *Phys. Rev. B* 75: 184103–184107.
13. Cui Y X, Wang Y M, Wen C, Ge B H, Li F H, Chen Y, and Chen H (2013) Determining polarity and dislocation core structures at atomic level for epitaxial aln/(0001)6h-sic from a single image in hrtem. *Ultramicroscopy*. 126: 77–84.
14. Cochran W (1955) Relations between the phases of structure factors. *Acta Crystallogr.* 8: 473–478.